

Chapter 2

Analytical Study on Hydrodynamic Characteristics

In this chapter, an analytical model is developed for the motion response and wave attenuation of a raft-type wave-powered desalination device. The desalination module of the device is simplified as a Power Take-Off (PTO) system. The analytical solution of diffraction and radiation problem of multiple two-dimensional rectangular bodies floating on a layer of water of finite depth is obtained using a linearized potential flow theory. Wave excitation forces, added masses and wave damping coefficients for these bodies are calculated from incident, diffracted and radiated potentials. Upon solving the motion equation, response, power absorption and wave attenuation of a raft-type wave power device are obtained. The model is validated by comparison of the present results with the existing ones, and energy conservation is checked. The validated model is then utilized to examine the effect of PTO damping coefficient, raft draft, spacing between two rafts, water depth, and raft numbers on power absorption and wave transmission coefficient of raft-type wave power device. The influence of structure length ratio is also discussed. It is found that the same wave transmission coefficient can be obtained by any certain raft-type wave power device, regardless of wave propagation direction.

2.1 Brief Introduction

Over the past decade, the demand for space and resources has increased significantly and the development toward ocean has already been an irresistible trend for residential purposes, industrial and logistic uses (Lamas-Pardo et al. 2015). This promotes the applications of floating structures in the ocean, such as floating farms, floating fuel storage facilities, floating bridges, floating stadia, floating hotels, floating airports and ports, as well as floating breakwaters and some wave energy converters, and consequently triggers extensive theoretical and experimental studies. Some of these floating structures can generally be defined as a system consisting of multiple floating (or fixed) bodies connected by rigid or flexible

constraints. For such a system with an irregular configuration, numerical methods might be the only way to analyze the wave diffraction and radiation within the framework of potential flow theory. On the other hand, an analytical analysis might be possible for the structures with a regular configuration, such as a series of linked rectangular floats.

Up to date, diffracted and radiated problems of wave interaction with floating structures of rectangular cross section have been extensively studied. Haren (1978) presented a two-dimensional (2-D) analytical model using the linearized shallow water theory for a wave power device which consists of a train of floating rafts linked together by hinges. The wave-induced rotation around the hinges is used to generate energy. For the raft train in deep water, a numerical model based on a hybrid element method for arbitrary wavelength was also applied. McIver (1986) investigated the enhancement of wave forces due to the interaction effect between two adjacent parallel floating bridges using the method of matched eigen-function expansions. The results showed the possibility of very large resonant motions but with a very narrow bandwidth for the frequencies of interest. Williams and Abul-Azm (1997) studied the behavior of a dual pontoon breakwater, which consists of a pair of moored rectangular pontoons supporting a rigid deck. It was shown that the dual pontoon breakwater may exhibit better wave reflection characteristics than a single pontoon structure with the same overall dimensions. A numerical model based on the boundary integral equation method and an appropriate Green's function was presented by Williams et al. (2000) to investigate the hydrodynamic properties of a pair of moored floating pontoon breakwaters of rectangular section. The two structures are not connected in any way, and move independently. It was found that there was an obvious effect of the spacing between the two pontoons on wave reflection properties of the structures. Miao et al. (2000) adopted a reduced two dimensional source distribution method for systematic computations on the interaction between waves and twin or more adjacent caissons. A series of pulsating sources at each gap end were introduced to simulate the gap influence. For twin surface rectangular obstacles in a finite depth of water, Li et al. (2005) applied a novel numerical method called the modified scaled boundary finite element method (SBFEM) to solve the wave diffraction and wave radiation problem. Lu et al. (2011) made a comparison between a viscous fluid model and a potential flow model in solving the 2-D problem of wave forces acting on multiple floating bodies in close proximity. It was shown that the conventional potential flow model worked well in predicting the response frequency of wave forces acting on each floating bodies. More recently, Liu and Li (2014) gave a solution for gap resonance between twin fixed floating rectangular boxes. Energy dissipation was introduced into the dissipative domain by adding an artificial resistance force, therefore a better prediction of the free surface response was obtained.

The majority of above works are limited to numerical investigation into the hydrodynamic problem of raft-type wave power devices, and to the best of the author's knowledge, there is no work to study the hydrodynamic characteristics of linked floats using an analytical method with consideration of spacing distance effect. Since the preparation of all data set for a numerical experiment is very

tedious, the analytical method, which is sufficient and effective for ideal analysis, may be more suitable to optimize a raft type wave power device and investigate its response. In this chapter, the author presents an analytical model for the motion response and wave attenuation of a raft-type wave power device, which contains a series of hinged rectangular floats, floating on a layer of water of finite depth with waves. The effects of multiple parameters such as linear damping coefficient, raft length, draft, spacing distance, float length ratio and float numbers on wave power absorption and wave transmission coefficient are examined.

2.2 Analytical Model

Consider a raft wave power device, consisting of multiple rigid rectangular floating structures connected together by the joints between each other, floating in water of finite depth, as shown in Fig. 2.1. Seawater desalination system is assumed as Power Take-Off (PTO) dampers installed at the joints to capture the power absorbed by these structures from waves.

To make a convenient description of the problem, a Cartesian coordinate (x , y , z) system is introduced, in which the x , y and z axes are defined as the wave propagation, wave crest-line and upward directions, respectively, with the origin on the undisturbed free surface. The width of all the floating structures in the y direction is assumed to be far longer than a wave length so that the diffraction and radiation problem can be treated as two-dimensional one. As shown in Fig. 2.1, the raft-type device is subjected to a monochromatic incident wave train of small amplitude A and frequency ω propagating along the x axis in the water area of a constant depth of h . For convenience of description, all the rectangular structures of the device are numbered from left to right in ascending order, 1, 2, ..., N . The total number of rectangular structures is N ($N > 1$), the length and immersion depth of the n -th structure as well as the spacing between the n -th structure and the $(n + 1)$ -th structure are a_n , d_n and D_n , respectively. The horizontal positions of the left wall

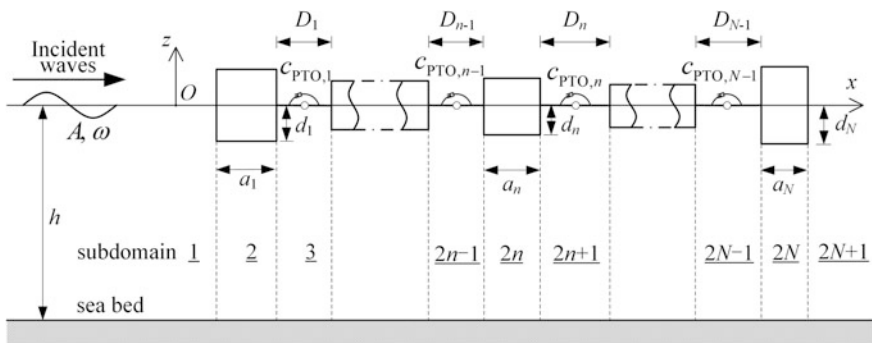
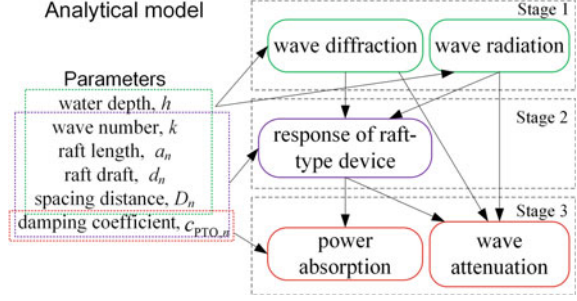


Fig. 2.1 Schematic of a raft wave power device consisting of multiple hinged *rectangular* floating structures

Fig. 2.2 Flow chart of analytical model development



and right wall of the n -th structure are denoted by $X_{l,n}$ and $X_{r,n}$, respectively, in which subscripts l and r before a comma denote the left and right wall position of the n -th structure ($n = 1, 2, \dots, N$), respectively. The rotation center of the n -th structure is (x_n, z_n) ($n = 1, 2, \dots, N$), which is used as a reference point to calculate the wave moment, added mass and radiation damping relative to rotation mode. The joint between the n -th structure and the $(n + 1)$ -th structure is located at the middle of the still water surface between these two structures with the rotary damping coefficient written as $c_{PTO,n}$ ($n = 1, 2, \dots, N - 1$).

An analytical model is developed for the motion response and wave attenuation of the raft-type wave power device in a sequential approach, as shown in Fig. 2.2. The diffraction and radiation problem of multiple two-dimensional rectangular bodies floating on a layer of water of finite depth with waves should first be solved in Stage 1. Wave excitation forces, added masses and wave damping coefficients for these bodies can be calculated from incident, diffracted and radiated potentials. After solving the equation of motion based on the results of diffraction and radiation problem, response, power absorption and wave attenuation of a raft-type wave power device are obtained in Stage 2 and Stage 3, respectively.

2.2.1 Diffraction and Radiation Problem

Assuming that the fluid is isotropic and incompressible inviscid, the time-harmonic flow is irrotational, the deformation of each structure is very small and can be neglected, the hydrodynamic problem may be treated by using the potential theory in the frequency domain. The fluid motion can be described by the velocity potential $\Phi(x, z, t) = \text{Re}[\varphi(x, z)e^{-i\omega t}]$, where t is the time; $i = \sqrt{-1}$; φ is a complex spatial velocity potential independent of time which satisfies the Laplace equation:

$$\frac{\partial^2 \varphi}{\partial x^2} + \frac{\partial^2 \varphi}{\partial z^2} = 0. \quad (2.1)$$

Suffering from waves with small wave amplitude, motion response of each raft could be small as well. Therefore, the spatial velocity potential φ can be

decomposed into an incident wave spatial potential φ_I , a diffracted wave spatial potential φ_D and a radiated wave spatial potential $\varphi_{R,p}^{(n)}$:

$$\varphi = \varphi_I + \varphi_D - i\omega \sum_{n=1}^N \sum_{p=1}^3 X_p^{(n)} \varphi_{R,p}^{(n)}, \quad (2.2)$$

where $X_p^{(n)}$ is the complex amplitude of the n -th structure motion in mode p ; $\varphi_{R,p}^{(n)}$ is the spatial velocity potential due to unit amplitude velocity oscillation of the n -th structure in mode p . In this chapter for 2-D problems, the superscript p is the p -th mode in which p is 1, 2 and 3, standing for the surge, heave and pitch modes, respectively; subscripts I, D and R denote quantities of incident, diffracted and radiated waves, respectively. It should be pointed out that these three spatial potentials all satisfy the Laplace equation as shown in Eq. (2.1).

Generally, the spatial velocity potential for undisturbed incident waves with amplitude A propagating along x direction can be written as:

$$\varphi_I = -\frac{igA \cosh[k(z+h)]}{\omega \cosh(kh)} e^{ikx}, \quad (2.3)$$

where k is the wave number, which satisfies the dispersion relation $\omega^2 = gk \tanh(kh)$; g is the gravity acceleration.

Boundary conditions

For wave diffraction problem, all the floats are assumed to be fixed bodies being subjected to a regular incident wave train. The governing equation and its boundary conditions for the diffracted spatial potential can be written as follows:

$$\frac{\partial^2 \varphi_D}{\partial x^2} + \frac{\partial^2 \varphi_D}{\partial z^2} = 0, \quad \text{fluid domain} \quad (2.4)$$

$$\frac{\partial \varphi_D}{\partial z} - \frac{\omega^2}{g} \varphi_D = 0, \quad \text{free surface} \quad (2.5)$$

$$\frac{\partial \varphi_D}{\partial z} = 0, \quad \text{sea bed} \quad (2.6)$$

$$\frac{\partial \varphi_D}{\partial z} = -\frac{\partial \varphi_I}{\partial z}, \quad \text{raft bottom} \quad (2.7)$$

$$\frac{\partial \varphi_D}{\partial x} = -\frac{\partial \varphi_I}{\partial x}, \quad \text{raft side wall} \quad (2.8)$$

$$\varphi_D \text{ outgoing; finite value at infinite distance.} \quad (2.9)$$

Similarly, the radiation spatial velocity potential $\varphi_{R,p}^{(n)}$ satisfies the following boundary conditions:

$$\frac{\partial^2 \varphi_{R,p}^{(n)}}{\partial x^2} + \frac{\partial^2 \varphi_{R,p}^{(n)}}{\partial z^2} = 0, \quad \text{fluid domain} \quad (2.10)$$

$$\frac{\partial \varphi_{R,p}^{(n)}}{\partial z} - \frac{\omega^2}{g} \varphi_{R,p}^{(n)} = 0, \quad \text{free surface} \quad (2.11)$$

$$\frac{\partial \varphi_{R,p}^{(n)}}{\partial z} = 0, \quad \text{sea bed} \quad (2.12)$$

$$\frac{\partial \varphi_{R,p}^{(n)}}{\partial z} = \delta_{m,n} [\delta_{2,p} - (x - x_m) \delta_{3,p}], \quad \text{raft bottom} \quad (2.13)$$

$$\frac{\partial \varphi_{R,p}^{(n)}}{\partial x} = \delta_{m,n} [\delta_{1,p} + (z - z_m) \delta_{3,p}], \quad \text{raft side wall} \quad (2.14)$$

$$\varphi_{R,p}^{(n)} \text{ outgoing; finite value at infinite distance.} \quad (2.15)$$

where subscript m denotes the m -th structure; $\delta_{p,q}$ is the Kronecker delta, viz.

$$\delta_{p,q} = \begin{cases} 1 & p = q \\ 0 & p \neq q \end{cases}. \quad (2.16)$$

Solution to diffracted and radiated spatial potentials

From the comparison of two sets of governing equations for the diffracted and radiated spatial potentials shown in Eqs. (2.4)–(2.15), it is noted that this two sets of governing equations are all the same apart from the boundary conditions on the wetted surface of the rectangular structures. Therefore, the same method is applied to solve these two sets of equations. The eigen-function expansion matching method (Zheng et al. 2004; Zheng and Zhang 2016) is adopted to derive the analytical solutions of diffracted and radiated spatial potentials for multiple floating rectangular bodies. For N ($N > 1$) rectangular structures floating on water surface, the fluid domain is divided into $2N + 1$ subdomains as shown in Fig. 2.1. In the m -th subdomain Ω_m which is surrounded by its two adjacent dash-lines, sea bed and structure bottom/free surface, the diffracted spatial potential and radiated spatial potential due to unit amplitude velocity oscillation of the n -th structure in mode p are denoted by $\varphi_{D,m}$ and $\varphi_{R,p,m}^{(n)}$, respectively. The method of separation of variables is applied in each subdomain in order to obtain analytical expressions for unknown diffracted spatial potentials and radiated spatial potential.

Diffracted spatial potentials in subdomains

Utilizing the method of separation of variables, the diffracted spatial potential, satisfying Eqs. (2.4)–(2.7) and (2.9), in Subdomains 1, $2m$, $2m + 1$ and $2N + 1$ can be expressed, respectively, as:

$$\varphi_{D,1} = \sum_{j=1}^{\infty} A_{1,j}^D e^{\lambda_j x} \cos \Theta_j, \quad \text{in } \Omega_1 \quad (2.17)$$

$$\begin{aligned} \varphi_{D,2m} = & \varphi_{D,2m}^p + A_{2m,1}^D x + B_{2m,1}^D \\ & + \sum_{j=2}^{\infty} \left(A_{2m,j}^D e^{\beta_{m,j} x} + B_{2m,j}^D e^{-\beta_{m,j} x} \right) \cos [\beta_{m,j} (z + h)], \quad \text{in } \Omega_{2m} \end{aligned} \quad (2.18)$$

$$\varphi_{D,2m+1} = \sum_{j=1}^{\infty} \left(A_{2m+1,j}^D e^{\lambda_j x} + B_{2m+1,j}^D e^{-\lambda_j x} \right) \cos \Theta_j, \quad \text{in } \Omega_{2m+1}, \quad m \neq N \quad (2.19)$$

$$\varphi_{D,2N+1} = \sum_{j=1}^{\infty} A_{2N+1,j}^D e^{-\lambda_j x} \cos \Theta_j, \quad \text{in } \Omega_{2N+1} \quad (2.20)$$

where the terms with $j = 1$ are the propagating waves, whereas the terms with $j > 1$ are “evanescent waves”; $\Theta_j = \lambda_j (z + h)$; $A_{1,j}^D$, $A_{2m,j}^D$, $B_{2m,j}^D$, $A_{2m+1,j}^D$, $B_{2m+1,j}^D$ and $A_{2N+1,j}^D$ are the coefficients to be solved; $\varphi_{D,2m}^p$ is a particular solution in Subdomain $2m$, where superscript p is associated with particular solution. $\varphi_{D,2m}^p$ can be given by:

$$\varphi_{D,2m}^p = -\varphi_1, \quad (2.21)$$

$\beta_{m,j}$ and λ_j are the eigenvalues of the j -th wave modes in Subdomain $2m$, and the other subdomains, respectively, which are given by Falnes (2002):

$$\lambda_1 = -ik, \quad j = 1 \quad (2.22)$$

$$\omega^2 = -\lambda_j g \tan(\lambda_j h), \quad j = 2, 3, \dots \quad (2.23)$$

$$\beta_{m,j} = \frac{(j-1)\pi}{h - d_m}, \quad j = 1, 2, 3, \dots \quad (2.24)$$

For the two-dimensional case, Eq. (2.19) represents a general wave solution for the velocity potential in a uniform fluid of constant depth (Falnes 2002).

Radiated spatial potentials in subdomains

Similar to expressions for the diffracted spatial potentials, using the method of separation of variables, the radiated spatial velocity potentials for the n -th structure in the p -th mode satisfying Eqs. (2.10)–(2.13) and (2.15), in Subdomains 1, $2m$, $2m + 1$ and $2N + 1$, can be expressed, respectively, as

$$\varphi_{R,p,1}^{(n)} = \sum_{j=1}^{\infty} A_{p,1,j}^{(n)} e^{\lambda_j x} \cos \Theta_j, \quad \text{in } \Omega_1 \quad (2.25)$$

$$\begin{aligned} \varphi_{R,p,2m}^{(n)} &= \varphi_{R,p,2m}^{p,n} + A_{p,2m,1}^{(n)} x + B_{p,2m,1}^{(n)} \\ &+ \sum_{j=2}^{\infty} \left(A_{p,2m,j}^{(n)} e^{\beta_{m,j} x} + B_{p,2m,j}^{(n)} e^{-\beta_{m,j} x} \right) \cos [\beta_{m,j} (z + h)], \quad \text{in } \Omega_{2m} \end{aligned} \quad (2.26)$$

$$\varphi_{R,p,2m+1}^{(n)} = \sum_{j=1}^{\infty} \left(A_{p,2m+1,j}^{(n)} e^{\lambda_j x} + B_{p,2m+1,j}^{(n)} e^{-\lambda_j x} \right) \cos \Theta_j, \quad \text{in } \Omega_{2m+1}, \quad m \neq N \quad (2.27)$$

$$\varphi_{R,p,2N+1}^{(n)} = \sum_{j=1}^{\infty} A_{p,2N+1,j}^{(n)} e^{-\lambda_j x} \cos \Theta_j, \quad \text{in } \Omega_{2N+1} \quad (2.28)$$

where $A_{p,1,j}^{(n)}$, $A_{p,2m,j}^{(n)}$, $B_{p,2m,j}^{(n)}$, $A_{p,2m+1,j}^{(n)}$, $B_{p,2m+1,j}^{(n)}$ and $A_{p,2N+1,j}^{(n)}$ are the coefficients to be determined; $\varphi_{R,p,2m}^{p,n}$ is a particular solution in Subdomain $2m$, which is given by

$$\varphi_{R,p,2m}^{p,n} = \delta_{m,n} \left[\frac{(z+h)^2 - x^2}{2(h-d_m)} \delta_{2,p} - \frac{(z+h)^2 (x-x_m) - \frac{1}{3} (x-x_m)^3}{2(h-d_m)} \delta_{3,p} \right], \quad (2.29)$$

λ_j and $\beta_{m,j}$ are the eigenvalues defined by Eqs. (2.22)–(2.24).

Method of computation for coefficients

Equations (2.17)–(2.20) and (2.25)–(2.28) should satisfy the boundary conditions at the wet side walls as shown in Eqs. (2.8) and (2.14), respectively. In addition, at either the fluid-structure interface or the interface between two adjacent subdomains, the motion of the structures and fluids is fully coupled by velocities or pressures normal to the interface (Zhang 2010). At $x = x_{1,m}$ and $x = x_{r,m}$ ($n = 1, 2, \dots, N$), the velocities and pressures continuity conditions can be used to evaluate the $4N$ set of unknown coefficients as expressed in Eqs. (2.17)–(2.20) and (2.25)–(2.28).

The continuity conditions for diffracted spatial potentials are given as follows:

$$\frac{\partial \varphi_{D,2m-1}}{\partial x} = \begin{cases} -\frac{\partial \varphi_I}{\partial x} & (x = x_{l,m}, \quad -d_m < z < 0) \\ \frac{\partial \varphi_{D,2m}}{\partial x} & (x = x_{l,m}, \quad -h < z < -d_m) \end{cases}, \quad (2.30)$$

$$\frac{\partial \varphi_{D,2m+1}}{\partial x} = \begin{cases} -\frac{\partial \varphi_I}{\partial x} & (x = x_{r,m}, \quad -d_m < z < 0) \\ \frac{\partial \varphi_{D,2m}}{\partial x} & (x = x_{r,m}, \quad -h < z < -d_m) \end{cases}, \quad (2.31)$$

$$\varphi_{D,2m-1} = \varphi_{D,2m} \quad (x = x_{l,m}, \quad -h < z < -d_m), \quad (2.32)$$

$$\varphi_{D,2m} = \varphi_{D,2m+1} \quad (x = x_{r,m}, \quad -h < z < -d_m). \quad (2.33)$$

Similarly, the continuity conditions for the radiated spatial potentials are expressed as

$$\frac{\partial \varphi_{R,p,2m-1}^{(n)}}{\partial x} = \begin{cases} \delta_{m,n} [\delta_{1,p} + (z - z_m) \delta_{3,p}] & (x = x_{l,m}, \quad -d_m < z < 0) \\ \frac{\partial \varphi_{R,p,2m}^{(n)}}{\partial x} & (x = x_{l,m}, \quad -h < z < -d_m) \end{cases}, \quad (2.34)$$

$$\frac{\partial \varphi_{R,p,2m+1}^{(n)}}{\partial x} = \begin{cases} \delta_{m,n} [\delta_{1,p} + (z - z_m) \delta_{3,p}] & (x = x_{r,m}, \quad -d_m < z < 0) \\ \frac{\partial \varphi_{R,p,2m}^{(n)}}{\partial x} & (x = x_{r,m}, \quad -h < z < -d_m) \end{cases}, \quad (2.35)$$

$$\varphi_{R,p,2m-1}^{(n)} = \varphi_{R,p,2m}^{(n)} \quad (x = x_{l,m}, \quad -h < z < -d_m), \quad (2.36)$$

$$\varphi_{R,p,2m}^{(n)} = \varphi_{R,p,2m+1}^{(n)} \quad (x = x_{r,m}, \quad -h < z < -d_m). \quad (2.37)$$

The continuity conditions above are satisfied over the z interval in a least-square sense by multiplying both sides of them by their corresponding eigen-function in their subdomains and then by integrating them over their corresponding intervals at the boundaries $x = X_{l,m}$ and $x = X_{r,m}$. The procedure above gives the following equations for diffracted spatial potentials:

$$\int_{-h}^0 \frac{\partial \varphi_{D,2m-1}}{\partial x} \cos \Theta_i dz = - \int_{-d_m}^0 \frac{\partial \varphi_I}{\partial x} \cos \Theta_i dz + \int_{-h}^{-d_m} \frac{\partial \varphi_{D,2m}}{\partial x} \cos \Theta_i dz, \quad x = x_{l,m} \quad (2.38)$$

$$\int_{-d_m}^0 -\frac{\partial \varphi_I}{\partial x} \cos \Theta_i dz + \int_{-h}^{-d_m} \frac{\partial \varphi_{D,2m}}{\partial x} \cos \Theta_i dz = \int_{-h}^0 \frac{\partial \varphi_{D,2m+1}}{\partial x} \cos \Theta_i dz, \quad x = x_{r,m} \quad (2.39)$$

$$\int_{-h}^{-d_m} \varphi_{D,2m-1} \cos[\beta_{m,i}(z+h)] dz = \int_{-h}^{-d_m} \varphi_{D,2m} \cos[\beta_{m,i}(z+h)] dz, \quad x = x_{l,m} \quad (2.40)$$

$$\int_{-h}^{-d_m} \varphi_{D,2m} \cos[\beta_{m,i}(z+h)] dz = \int_{-h}^{-d_m} \varphi_{D,2m+1} \cos[\beta_{m,i}(z+h)] dz, \quad x = x_{r,m} \quad (2.41)$$

and the equations for radiated spatial potentials:

$$\begin{aligned} \int_{-h}^0 \frac{\partial \varphi_{R,p,2m-1}^{(n)}}{\partial x} \cos \Theta_i dz &= \int_{-d_m}^0 \delta_{m,n} [\delta_{1,p} + (z - z_m) \delta_{3,p}] \cos \Theta_i dz \\ &+ \int_{-h}^{-d_m} \frac{\partial \varphi_{R,p,2m}^{(n)}}{\partial x} \cos \Theta_i dz, \quad x = x_{l,m} \end{aligned} \quad (2.42)$$

$$\begin{aligned} &\int_{-d_m}^0 \delta_{m,n} [\delta_{1,p} + (z - z_m) \delta_{3,p}] \cos \Theta_i dz + \int_{-h}^{-d_m} \frac{\partial \varphi_{R,p,2m}^{(n)}}{\partial x} \cos \Theta_i dz \\ &= \int_{-h}^0 \frac{\partial \varphi_{R,p,2m+1}^{(n)}}{\partial x} \cos \Theta_i dz, \quad x = x_{r,m} \end{aligned} \quad (2.43)$$

$$\begin{aligned} &\int_{-h}^{-d_m} \varphi_{R,p,2m-1}^{(n)} \cos[\beta_{m,i}(z+h)] dz \\ &= \int_{-h}^{-d_m} \varphi_{R,p,2m}^{(n)} \cos[\beta_{m,i}(z+h)] dz, \quad x = x_{l,m} \end{aligned} \quad (2.44)$$

$$\begin{aligned} &\int_{-h}^{-d_m} \varphi_{R,p,2m}^{(n)} \cos[\beta_{m,i}(z+h)] dz \\ &= \int_{-h}^{-d_m} \varphi_{R,p,2m+1}^{(n)} \cos[\beta_{m,i}(z+h)] dz, \quad x = x_{r,m} \end{aligned} \quad (2.45)$$

Upon substituting Eqs. (2.17)–(2.20) with diffraction unknown coefficients and Eqs. (2.25)–(2.28) with radiation unknown coefficients into Eqs. (2.38)–(2.41) and (2.42)–(2.45), respectively, and taking the first M terms in the infinite series, two sets of linear system of $4 \times M \times N$ complex equations with the same number of unknown coefficients are obtained. The diffracted spatial potentials and the radiated spatial potentials in each subdomain can be easily obtained by solving these complex equations. In general, whether more floats or more truncated eigen-function terms of the infinite series means more time needed to solve the diffraction and radiation problem (Zheng and Zhang 2016).

Wave forces and hydrodynamic coefficients

Wave excitation forces are ones due to incident wave acting on structures which are stationary, and can be computed from the incident wave potential and the diffracted wave potential. The generalized excitation force on the n -th structure in mode p is $\text{Re}[F_{e,p}^{(n)}e^{-i\omega t}]$, in which

$$F_{e,p}^{(n)} = -i\omega\rho \int_{S_n} (\varphi_I + \varphi_D)n_p ds, \quad (2.46)$$

where S_n is the wetted surface of the n -th structure; $\vec{n} = n_x\vec{i} + n_z\vec{j}$ is the unit normal vector directed into the fluid domain at the considered buoy surface; n_p is the generalized normal with $n_1 = n_x$, $n_2 = n_z$, $n_3 = (z - z_n)n_x - (x - x_n)n_z$.

Excitation forces acting on each rafts can be calculated directly by substituting the expressions of incident and diffracted spatial potentials into Eq. (2.46).

The radiation force acting on m -th structure in mode p is written as $\text{Re}[F_{R,p}^{(m)}e^{-i\omega t}]$, in which

$$\begin{aligned} F_{R,p}^{(m)} &= -\omega^2\rho \sum_{n=1}^N \sum_{q=1}^3 X_q^{(n)} \int_{S_m} \varphi_{R,q}^{(n)} n_p ds \\ &= \sum_{n=1}^N \sum_{q=1}^3 \omega^2 X_q^{(n)} a_{p,q}^{m,n} + \sum_{n=1}^N \sum_{q=1}^3 i\omega X_q^{(n)} c_{p,q}^{m,n}, \end{aligned} \quad (2.47)$$

where $a_{p,q}^{m,n}$ and $c_{p,q}^{m,n}$ are the added mass and radiation damping coefficients, respectively, of the m -th structure in mode p due to the n -th structure unit velocity oscillation motion in mode q .

2.2.2 Response of Raft-Type Device

For the motion response problem of multiple hinged rafts, once upon obtaining the wave excitation forces and hydrodynamic coefficients of each floating structure, the complex amplitude of each structure motion in each mode can be calculated immediately (Zheng et al. 2015a, b; Zheng and Zhang 2017)

$$\begin{bmatrix} -\omega^2(\mathbf{M} + \mathbf{M}_a) - i\omega(\mathbf{C}_d + \mathbf{C}_{PTO}) + \mathbf{K}_s & \mathbf{A}_J^T \\ \mathbf{A}_J & \mathbf{0} \end{bmatrix} \begin{Bmatrix} \mathbf{X} \\ \mathbf{F}_J \end{Bmatrix} = \begin{Bmatrix} \mathbf{F}_e \\ \mathbf{0} \end{Bmatrix}, \quad (2.48)$$

in which \mathbf{M} and \mathbf{K}_s are the mass matrix and hydrostatic stiffness matrix of the multi-structures system, respectively; \mathbf{M}_a and \mathbf{C}_d are the added mass and wave damping matrices of the multiple floating structures, respectively; \mathbf{X} and \mathbf{F}_e are the

response motion vector and wave excitation force vector of the multi-structures system, separately; \mathbf{A}_J is the joint displacement constraint matrix; \mathbf{F}_J is the joint force vector; \mathbf{C}_{PTO} is PTO damping matrix. \mathbf{A}_J and \mathbf{C}_{PTO} can be written as:

$$\mathbf{A}_J = \begin{bmatrix} 1 & 0 & 0 & 0 & 0 & 0 & 0 \\ 0 & 1 & 0 & 0 & 0 & 0 & 0 \\ 0 & -\frac{a_1+D_1}{2} & 0 & 0 & 0 & 0 & 0 \\ -1 & 0 & 1 & 0 & 0 & 0 & 0 \\ 0 & -1 & 0 & 1 & 0 & 0 & 0 \\ 0 & -\frac{a_2+D_1}{2} & 0 & -\frac{a_2+D_2}{2} & \dots & & \\ & & & \vdots & & 0 & 0 \\ 0 & 0 & 0 & 0 & 0 & -1 & 0 \\ 0 & 0 & 0 & 0 & 0 & 0 & -1 \\ 0 & 0 & 0 & 0 & 0 & 0 & -\frac{a_N+D_{N-1}}{2} \end{bmatrix}^T, \quad (2.49)$$

$3N \times (2N-2)$

$$\mathbf{C}_{PTO} = \begin{bmatrix} 0 & 0 & 0 & 0 & 0 & 0 & 0 & 0 & 0 & 0 \\ 0 & 0 & 0 & 0 & 0 & 0 & 0 & 0 & 0 & 0 \\ 0 & 0 & c_{PTO,1} & 0 & 0 & -c_{PTO,1} & 0 & 0 & 0 & 0 \\ 0 & 0 & 0 & 0 & 0 & 0 & 0 & 0 & 0 & 0 \\ 0 & 0 & 0 & 0 & 0 & 0 & 0 & 0 & 0 & 0 \\ 0 & 0 & -c_{PTO,1} & 0 & 0 & c_{PTO,1} + c_{PTO,2} & 0 & 0 & -c_{PTO,2} & 0 \\ & & & \vdots & & & & & & \\ 0 & 0 & 0 & 0 & 0 & 0 & c_{PTO,N-2} + c_{PTO,N-1} & 0 & 0 & -c_{PTO,N-1} \\ 0 & 0 & 0 & 0 & 0 & 0 & 0 & 0 & 0 & 0 \\ 0 & 0 & 0 & 0 & 0 & 0 & 0 & 0 & 0 & 0 \\ 0 & 0 & 0 & 0 & 0 & 0 & -c_{PTO,N-1} & 0 & 0 & c_{PTO,N-1} \end{bmatrix} \quad (2.50)$$

$3N \times 3N$

2.2.3 Power Absorption Efficiency, Reflection and Transmission Coefficients

The average power that the device captures through the PTO system from regular waves can be written as:

$$P = \frac{1}{2} \omega^2 \sum_{n=1}^{N-1} c_{PTO,n} \left| X_3^{(n+1)} - X_3^{(n)} \right|^2. \quad (2.51)$$

The incoming wave power per unit width of the wave front, P_{in} is given by:

$$P_{in} = \frac{\rho g A^2 \omega}{2 \cdot 2k} \left[1 + \frac{2kh}{\sinh(2kh)} \right]. \quad (2.52)$$

The average power capture efficiency η for 2-D problem is calculated as:

$$\eta = \frac{P}{P_{\text{in}}}. \quad (2.53)$$

Floating structures can be seen as wave barriers or breakwater. The reflection and transmission coefficients R_w and T_w , which are indicative of the performance of the breakwater, can be obtained by computing the wave amplitudes at radiation boundary far away from these multiple structures. The complex amplitude of the transmission coefficient of floating hinged structures, \hat{T}_w , can be expressed as:

$$\hat{T}_w = \hat{T}_{w,0} + \frac{\omega^2 \cosh(kh)}{Ag} \mathbf{X}^T \mathbf{A}^+, \quad \hat{T}_{w,0} = 1 - \frac{\omega \cosh(kh)}{iAg} A_{2N+1,1}^D e^{-ikx_{r,N}}, \quad (2.54)$$

where $\hat{T}_{w,0}$ is the transmission coefficient of the raft device without any motions in the water; $\mathbf{A}^+ = e^{-ikx_{r,N}} [A_{1,2N+1,1}^{(1)}, A_{2,2N+1,1}^{(1)}, A_{3,2N+1,1}^{(1)}, A_{1,2N+1,1}^{(2)}, A_{2,2N+1,1}^{(2)}, A_{3,2N+1,1}^{(2)}, \dots, A_{3,2N+1,1}^{(N)}]^T$.

Correspondingly, the reflection coefficient of the raft device, \hat{R}_w , is

$$\hat{R}_w = \frac{\omega \cosh(kh)}{iAg} \left(A_{1,1}^D e^{ikx_{l,1}} - i\omega \mathbf{X}^T \mathbf{A}^- \right), \quad (2.55)$$

where $\mathbf{A}^- = e^{ikx_{l,1}} [A_{1,1,1}^{(1)}, A_{2,1,1}^{(1)}, A_{3,1,1}^{(1)}, A_{1,1,1}^{(2)}, A_{2,1,1}^{(2)}, A_{3,1,1}^{(2)}, \dots, A_{3,1,1}^{(N)}]^T$.

2.3 Model Validation

To validate the above-derived analytical model for diffracted spatial potentials, radiated spatial potentials, excitation forces, added mass, radiation damping, wave reflection and transmission coefficients and power absorption efficient, as expressed in Sect. 2.2, in this section several published examples are carried out by using the present model. Analytical results are then compared with the published data. In our computations, the first 50 terms in the infinite series of the diffracted spatial potentials and radiated spatial potentials are taken. To make it convenient to compare the analytical results with published data, the excitation forces, hydrodynamic coefficients and some physical and geometric parameters are normalized as follows:

$$\bar{F}_{e,p}^{(n)} = \frac{|F_{e,p}^{(n)}|}{\rho g h A}, \quad p = 1, 2; \quad \bar{F}_{e,3}^{(n)} = \frac{|F_{e,3}^{(n)}|}{\rho g h A a_n} \quad (2.56)$$

$$\bar{a}_{p,q}^{m,n} = \frac{a_{p,q}^{m,n}}{\rho h a_m}, \quad \bar{c}_{p,q}^{m,n} = \frac{c_{p,q}^{m,n}}{\omega \rho h a_m} \quad p = 1, 2; q = 1, 2 \quad (2.57)$$

$$\bar{a}_{p,q}^{m,n} = \frac{a_{p,q}^{m,n}}{\rho h a_m^2}, \quad \bar{c}_{p,q}^{m,n} = \frac{c_{p,q}^{m,n}}{\omega \rho h a_m^2} \quad p = 3; q = 1, 2 \text{ or } p = 1, 2; q = 3 \quad (2.58)$$

$$\bar{a}_{p,q}^{m,n} = \frac{a_{p,q}^{m,n}}{\rho h a_m^3}, \quad \bar{c}_{p,q}^{m,n} = \frac{c_{p,q}^{m,n}}{\omega \rho h a_m^3} \quad p = 3; q = 3 \quad (2.59)$$

$$\bar{h} = \frac{h}{L}, \quad \bar{a}_n = \frac{a_n}{L}, \quad \bar{D}_n = \frac{D_n}{L}, \quad \bar{d}_n = \frac{d_n}{L}, \quad \bar{c}_n = \frac{c_{\text{PTO},n} \sqrt{g h}}{\rho g L^4}, \quad \bar{T} = T \sqrt{\frac{g}{h}} \quad (2.60)$$

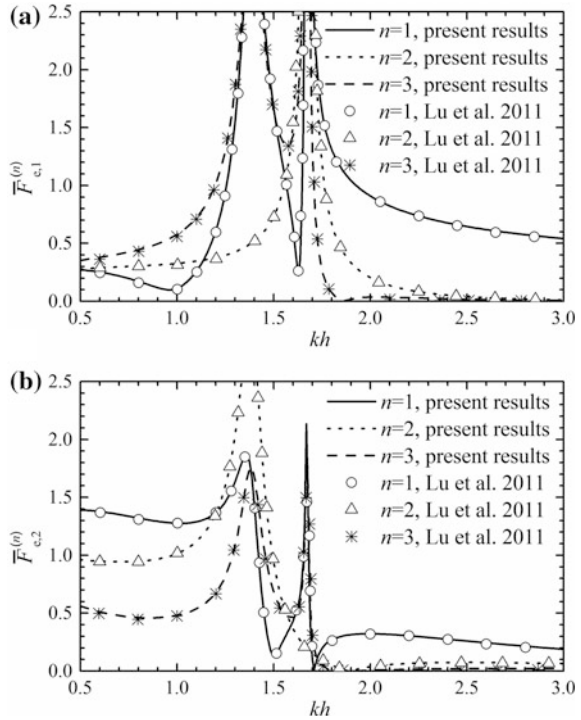
where L is a horizontal length scale. For the device floats with the same length scale, the float length can be seen as L ($L = a_n$). Otherwise, the water depth will be used as a scaling length ($L = h$).

In the first example, the horizontal and vertical wave excitation forces of three rectangular structures have been computed by Lu et al. (2011) by using both viscous fluid and potential flow models. The geometric parameters used by Lu et al. (2011) are $a_1/h = a_2/h = a_3/h = 1$, $D_1/h = D_2/h = 0.1$ and $d_1/h = d_2/h = d_3/h = 0.504$. Figure 2.3 shows the results of dimensionless magnitudes of surge and heave wave excitation forces acting on these three rectangular structures. It can be seen that there is a good agreement between our analytical results and those obtained by Lu et al. (2011) using numerical models based on potential flow. Such a good agreement indicates that the diffracted potentials presented here for the case of multiple rectangular structures are correct.

However, Lu et al. (2011) did not calculate the radiated potential, and neither added mass nor radiation damping was given. In order to further verify the correctness of the radiated spatial potentials, the second example is taken from Williams et al. (2000) who obtained the numerical results of the radiation problem of a pair of long floating pontoon breakwaters of rectangular section by using the boundary integral equation method and an appropriate Green's function. In this example, the geometric parameters are $a_1/h = a_2/h = 0.4$, $D_1/h = 0.4$, $d_1/h = d_2/h = 0.1$. The hydrodynamic coefficients of this example for two rectangular structures are given in Figs. 2.4 and 2.5, which show that the results obtained by using the present analytical model agree well with those obtained by using the numerical model of Williams et al. (2000).

Equations (2.54) and (2.55) as shown in Sect. 2.2.3 can be used to evaluate the wave reflection and transmission coefficients for fixed multiple floats as well if only we set $\mathbf{X} = \mathbf{0}$. For this case, an experimental study of double fixed bodies was performed by Koutandos et al. (2005). The basic parameters of their experiment are

Fig. 2.3 Dimensionless magnitudes of surge and heave wave excitation forces on three identical bodies for $\bar{a}_1 = \bar{a}_2 = \bar{a}_3 = 1.0$, $\bar{h} = 1.0$, $\bar{D}_1 = \bar{D}_2 = 0.1$, $\bar{d}_1 = \bar{d}_2 = \bar{d}_3 = 0.504$: **a** surge wave excitation forces; **b** heave wave excitation forces



as: $\bar{a}_1 = \bar{a}_2 = 1.0$, $\bar{h} = 1.0$, $\bar{D}_1 = 4.25$, $\bar{d}_1 = \bar{d}_2 = 0.25$. Figure 2.6 shows the reflection and transmission coefficients for the same case obtained by using the present analytical model together with the experimental data (Koutandos et al. 2005). It can be seen that there is a good agreement between the present results and the experimental data.

Haren (1978) applied numerical method to calculate power absorption efficiency of three interconnected floats with no gaps between each other. The geometric parameters of this case are $\bar{a}_1 = 0.4375$, $\bar{a}_2 = 1.4375$, $\bar{a}_3 = 1.875$, $\bar{h} = 1.0$, and $\bar{d}_1 = \bar{d}_2 = \bar{d}_3 = 0.0075$. Figure 2.7 shows a comparison of analytical results obtained by using the present analytical model with the numerical results (Haren 1978), which gives a good agreement.

For a plane wave perpendicularly propagating upon a two-dimensional wave power device, apart from a reflected wave and a transmitted wave, which is propagating beyond the bodies, the power absorbed by the wave power device should also be counted as a part divided from the incident wave. From energy conservation arguments, it is to be expected that:

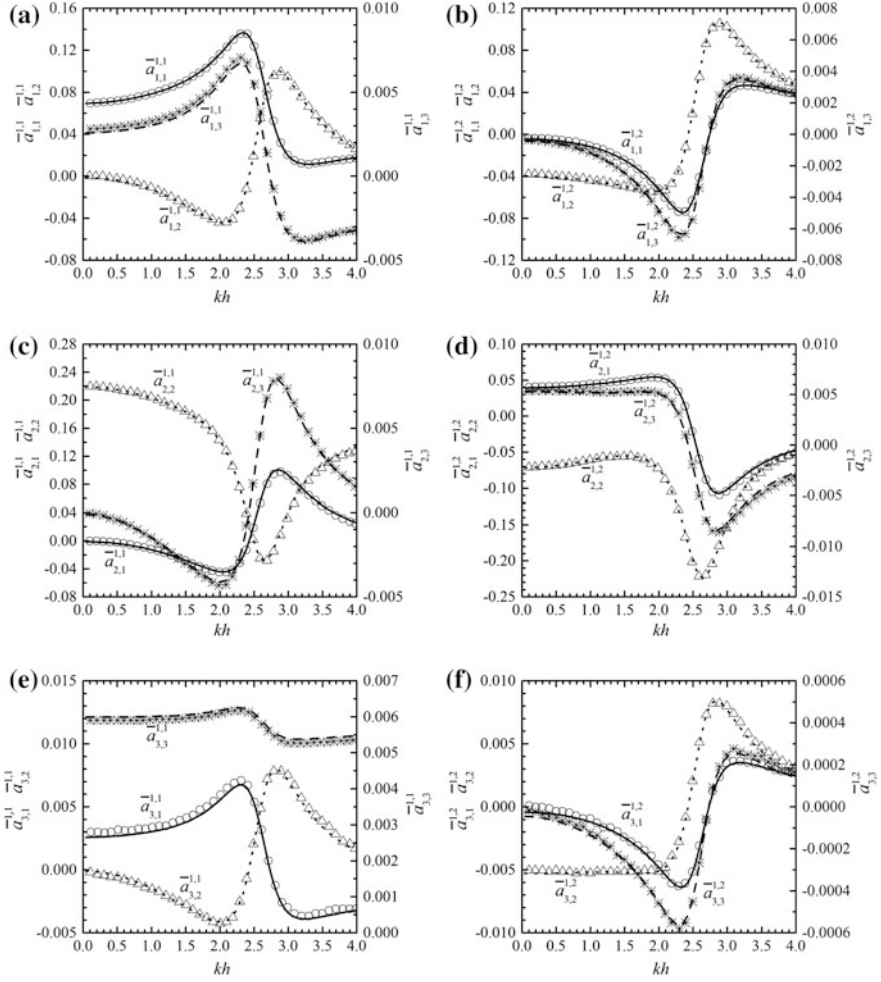


Fig. 2.4 Dimensionless surge, heave and pitch added-mass of structure 1 due to prescribed motions of structure 1 and 2 for $\bar{a}_1 = \bar{a}_2 = 1.0$, $\bar{h} = 2.5$, $\bar{D}_1 = 1.0$, $\bar{d}_1 = \bar{d}_2 = 0.25$: **a** surge added-mass due to motions of structure 1; **b** surge added-mass due to motions of structure 2; **c** heave added-mass due to motions of structure 1; **d** heave added-mass due to motions of structure 2; **e** pitch added-mass due to motions of structure 1; **f** pitch added-mass due to motions of structure 2. *Solid line* surge motion (present results); *dotted line* heave motion (present results); *dashed line* pitch motion (present results); *open circle* surge motion (Williams et al. 2000); *open triangle* heave motion (Williams et al. 2000); *asterisk* pitch motion (Williams et al. 2000)

$$R_w^2 + T_w^2 + \eta = 1. \quad (2.61)$$

That is to say, the energy extracted, plus the energy transmitted and reflected, should be equal to the incoming energy. Table 2.1 presents a series of analytical

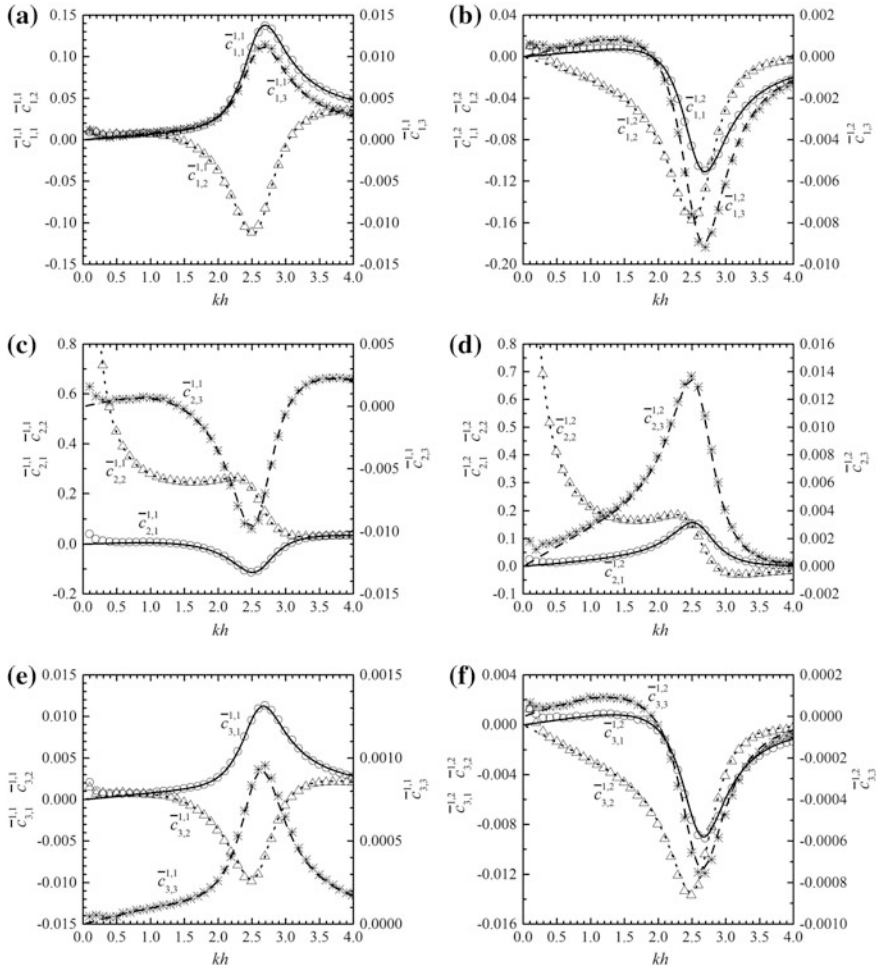


Fig. 2.5 Dimensionless surge, heave and pitch radiation damping of structure 1 due to prescribed motions of structures 1 and 2 for $\bar{a}_1 = \bar{a}_2 = 1.0$, $\bar{h} = 2.5$, $\bar{D}_1 = 1.0$, $\bar{d}_1 = \bar{d}_2 = 0.25$: **a** surge radiation damping due to motions of structure 1; **b** surge radiation damping due to motions of structure 2; **c** heave radiation damping due to motions of structure 1; **d** heave radiation damping due to motions of structure 2; **e** pitch radiation damping due to motions of structure 1; **f** pitch radiation damping due to motions of structure 2. *Solid line* surge motion (present results); *dotted line* heave motion (present results); *dashed line* pitch motion (present results); *open circle* surge motion (Williams et al. 2000); *open triangle* heave motion (Williams et al. 2000); *asterisk* pitch motion (Williams et al. 2000)

results of R_w , T_w and η for case a: $\bar{c}_1 = 0.005234$, $\bar{c}_2 = 0.01875$ under different wave conditions. It can be seen that the energy conservation arguments Eq. (2.61) is satisfied for all wave conditions.

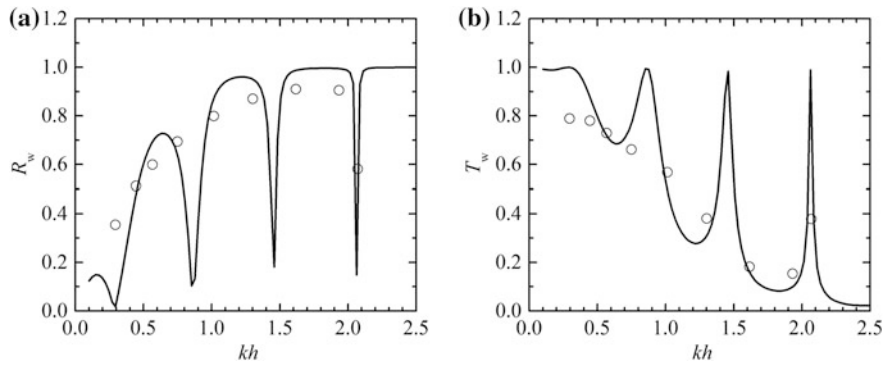


Fig. 2.6 Wave reflection and transmission coefficients for two fixed structures with $\bar{a}_1 = \bar{a}_2 = 1.0$, $\bar{h} = 1.0$, $\bar{D}_1 = 4.25$, $\bar{d}_1 = \bar{d}_2 = 0.25$, $A/h = 0.05$: **a** reflection coefficient; **b** transmission coefficient. Solid line present results; open circle experimental results with $A/h = 0.05$ (Koutandos et al. 2005)

Fig. 2.7 Variation of efficiency with nondimensional wave number for $\bar{h} = 1.0$, $\bar{a}_1 = 0.4375$, $\bar{a}_2 = 1.4375$, $\bar{a}_3 = 1.875$, $\bar{d}_1 = \bar{d}_2 = \bar{d}_3 = 0.0075$: train 1: $\bar{c}_1 = 0.005234$, $\bar{c}_2 = 0.01875$; train 2: $\bar{c}_1 = 0.003$, $\bar{c}_2 = 10^{-6}$; train 3: $\bar{c}_1 = 0.0033$, $\bar{c}_2 = 0.03$

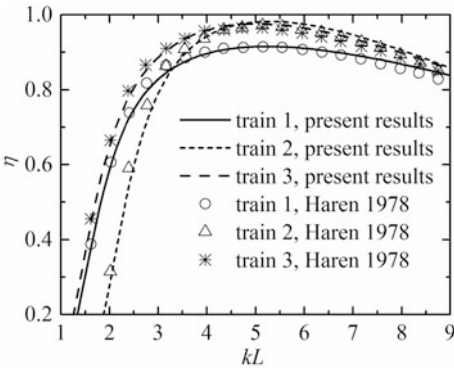


Table 2.1 Analytical results for train 1: $\bar{c}_1 = 0.005234$, $\bar{c}_2 = 0.01875$ with various values of kL

kL	R_w	T_w	η	$R_w^2 + T_w^2 + \eta$
0.2	0.00013	1.00000	0.00000	1.00000
1.0	0.02001	0.97348	0.05194	1.00000
1.8	0.19445	0.68852	0.48814	1.00000
2.6	0.27205	0.39806	0.76754	1.00000
3.4	0.26214	0.25753	0.86497	1.00001
4.2	0.25001	0.18587	0.90296	1.00001
5.0	0.25355	0.14407	0.91497	1.00001
5.8	0.27147	0.11703	0.91262	1.00001
6.6	0.29846	0.09819	0.90129	1.00001
7.4	0.33005	0.08433	0.88397	1.00002
8.2	0.36341	0.07372	0.86252	1.00002
9.0	0.39691	0.06532	0.83821	1.00002

2.4 Effects of Multiple Parameters

The performance of the multiple floating structures system as a wave energy converter and/or a wave barrier depends upon several parameters, the length, draft, distance between the structures, PTO damping and the number of structures. In this section, effects of these parameters on power absorption efficient and wave transmission coefficient are all investigated. Consider that the drafts of all rafts, the spacing distances between any two adjacent rafts and the linear damping coefficients at each joint are identical, respectively, \bar{d} , \bar{D} and \bar{c} are then introduced to represent the non-dimensional draft \bar{d}_n , non-dimensional spacing distance \bar{D}_n and non-dimensional linear damping coefficient \bar{c}_n at different joint(s) of the raft device, respectively with the purpose of only simplified description.

2.4.1 Linear PTO Damping

Linear damping coefficient is a key parameter affecting the power absorption of a wave power device. For a PTO damper of zero damping coefficient in a device, there would be no power absorbed either, whereas for a PTO damper of too large damping coefficient, the relative motion at the PTO system would be too small to generate electricity. Figure 2.8 shows how the efficiency and the transmission coefficient of the raft-type wave power device consisting of two rafts with $\bar{h} = 1.0$, $\bar{a}_1 = \bar{a}_2 = 1.0$, $\bar{d} = 0.05$, $\bar{D} = 0.05$ vary with nondimensional wave number kL and linear damping coefficient \bar{c} . It is shown in Fig. 2.8a that there are two peak values of efficiency for $kL = 0.1 \sim 15$ and $\bar{c} = 0 \sim 0.02$, one with a wide bandwidth occurs around $kL = 3.5$, whereas the other with a narrow one occurs at $kL = 11.2$. For $kL < 1.5$, as shown in Fig. 2.8b, the transmission coefficient is larger than 0.9

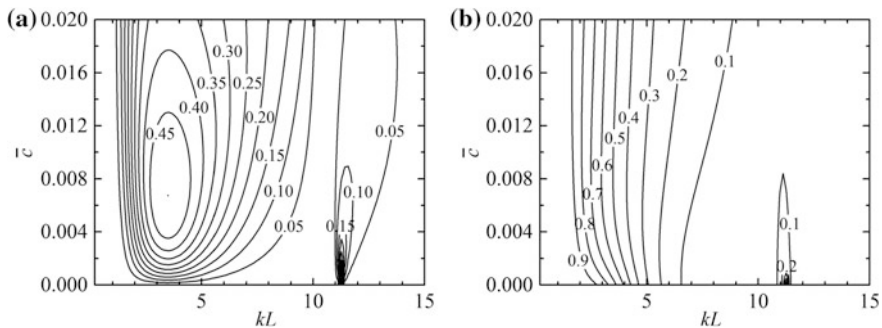


Fig. 2.8 Variation of efficiency and transmission coefficient with nondimensional wave number and linear damping coefficient for $\bar{h} = 1.0$, $\bar{a}_1 = \bar{a}_2 = 1.0$, $\bar{d} = 0.05$, $\bar{D} = 0.05$: **a** efficiency contour map; **b** transmission coefficient contour map

regardless of linear damping coefficient. For any certain linear damping coefficient, as kL increases from 0.1 to 10, the transmission coefficient decreases from 1 to the value smaller than 0.1. Similar to the efficiency, there is also a quite narrow peak of transmission coefficient at $kL = 11.2$.

2.4.2 Spacing Distance

The influence of spacing distance on the efficiency and the transmission coefficient is examined in this subsection. Figure 2.9 shows the variation of efficiency and transmission coefficient with nondimensional spacing distance and linear damping coefficient for $\bar{h} = 1.0$, $\bar{a}_1 = \bar{a}_2 = 1.0$, $\bar{d} = 0.05$, $\bar{T} = 3.5$. It seems that, for $\bar{T} = 3.5$, the spacing distance has a quite small influence on the behavior of the device. While for some other wave conditions, as shown in Fig. 2.10, the efficiency and transmission coefficient may be extremely affected by spacing distance.

For any specified raft-type wave power device in a certain wave condition, there would be a proper linear damping coefficient to maximize the power absorption efficiency, which can be called “optimal damping coefficient”. The curves shown in Fig. 2.10 represent the efficiency and transmission coefficient response for the device with various spacing distances and optimal damping coefficients at $\bar{T} = 3.5$. Each efficiency response curve illustrated in Fig. 2.10a shows a bimodal one with a zero value of efficiency between the two peaks. As kL increases from 0.1 to 3.5, the efficiency all monotonically increases from 0.0 to 0.5, regardless of spacing distance and the efficiency response curves for different spacing distances almost overlap each other for kL ranging from 0.1 to 4.0, leading to the same main peaks occur around $kL = 3.5$. The difference among these response curves for various \bar{D} tends to increase and then oscillates with increasing kL when $kL > 3.5$. A larger spacing distance results in a larger second peak value. What is more, as the spacing

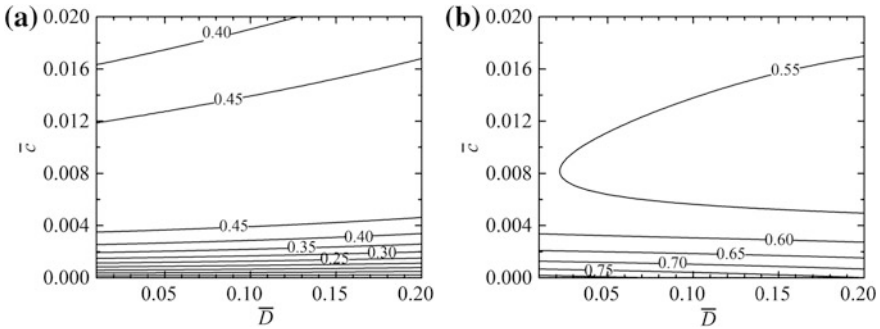


Fig. 2.9 Variation of efficiency and transmission coefficient with nondimensional spacing distance and linear damping coefficient for $\bar{h} = 1.0$, $\bar{a}_1 = \bar{a}_2 = 1.0$, $\bar{d} = 0.05$, $\bar{T} = 3.5$: **a** efficiency contour map; **b** transmission coefficient contour map

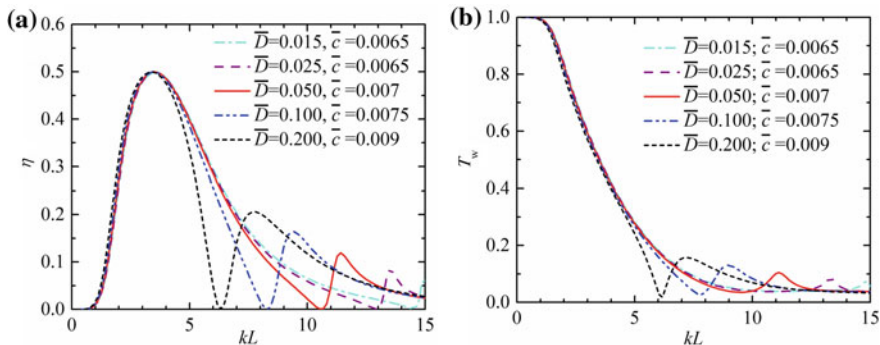


Fig. 2.10 Variation of efficiency and transmission coefficient with nondimensional wave number for different spacing distance and the optimal damping coefficient for $\bar{h} = 1.0$, $\bar{a}_1 = \bar{a}_2 = 1.0$, $\bar{d} = 0.05$: **a** efficiency; **b** transmission coefficient

distance increases, the second peak efficiency of the raft device and the zero value of efficiency response curves are both shifted to lower frequencies. This is due to the fact that the incident, diffracted and radiated waves act on the device floats simultaneously, and for a larger spacing distance, minor change in the incident wave frequency will lead to quick alteration of the phase difference between those waves. The tendency in the variation of transmission coefficient with kL as shown in Fig. 2.10b is quite different from those for efficiency response. As kL increases from 0.1 to 5.0, the transmission coefficient all monotonically decreases from 1.0 to about 0.3, regardless of spacing distance. As kL further increases, a small peak of transmission coefficient appears after reaching a minimum value. Figure 2.10b also shows the difference among transmission coefficient response curves for various \bar{D} , which is almost zero for $kL < 5.0$, and tends to increase and then oscillates with increasing kL for $kL > 5.0$. The larger the spacing distance, the lower frequencies where the peak transmission coefficient is shifted.

2.4.3 Draft

As the device usually needs to be equipped with an optimal weight, corresponding to an optimal raft draft, to obtain a maximum power absorption efficiency, it is necessary to examine the influence of draft on efficiency and transmission coefficient. Figure 2.11 shows the variation of efficiency and transmission coefficient with nondimensional draft \bar{d} and linear damping coefficient for $\bar{h} = 1.0$, $\bar{a}_1 = \bar{a}_2 = 1.0$, $\bar{D} = 0.05$ and $\bar{T} = 3.5$. For this certain wave condition, the maximum power absorption efficiency of the raft device reaches 0.50 when $\bar{d} = 0.079$ and $\bar{c} = 0.0056$ as shown in Fig. 2.11a. For $\bar{d} < 0.10$ and $\bar{c} < 0.004$, the power absorption efficiency is dramatically affected by the change of damping coefficient.

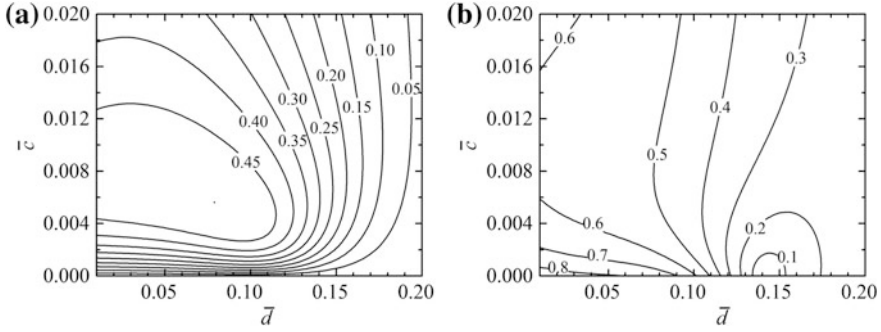


Fig. 2.11 Variation of efficiency and transmission coefficient with nondimensional draft and linear damping coefficient for $\bar{h} = 1.0$, $\bar{a}_1 = \bar{a}_2 = 1.0$, $\bar{D} = 0.05$, $\bar{T} = 3.5$: **a** efficiency contour map; **b** transmission coefficient contour map

While for $0.12 < \bar{d} < 0.20$ and $0.002 < \bar{c} < 0.020$, the power absorption efficiency is mainly influenced by \bar{d} rather than \bar{c} . As \bar{d} increases from 0.01 to 0.13, the transmission coefficient turns smaller and smaller as shown in Fig. 2.11b. The smallest value of the minimized transmission coefficient is less than 0.1, which occurs at $\bar{d} \approx 0.145$ with no damping.

Figure 2.12 presents the efficiency and transmission coefficient response curves for five drafts with their corresponding optimal linear damping coefficients at $\bar{T} = 3.5$. As shown in Fig. 2.12a, as \bar{d} increases from 0.015 to 0.1, although the optimal frequency which corresponds to the main peak of the efficiency response curves decreases slightly and the bandwidth also decreases, the peak value remains almost constant, being 0.5. However, the efficiency peak value for $\bar{d} = 0.2$ is only

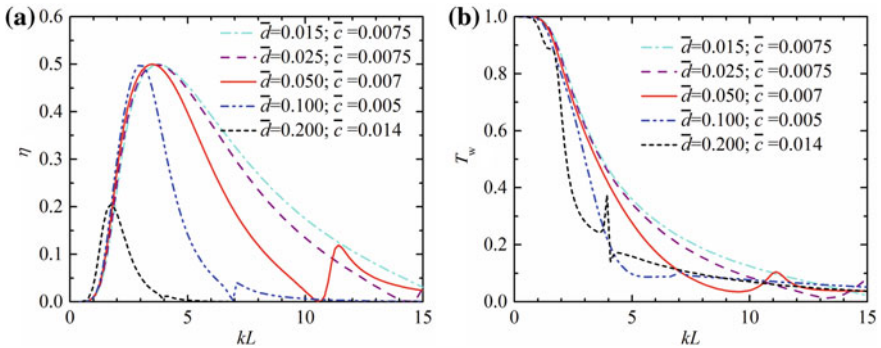


Fig. 2.12 Variation of efficiency and transmission coefficient with nondimensional wave number for different draft with the optimal damping coefficient for $\bar{h} = 1.0$, $\bar{a}_1 = \bar{a}_2 = 1.0$, $\bar{D} = 0.05$: **a** efficiency; **b** transmission coefficient

0.2, much less than those for smaller drafts. For long waves, for example $kL < 3.5$ as shown in Fig. 2.12b, the device with a large draft generally allows less energy to transmit the rafts.

2.4.4 Raft Numbers

Our previous discussion in Sects. 2.4.1–2.4.3 is focused on the performance of a wave power device with two hinged rafts. In order to see how the number of rafts influences on power absorption and wave attenuation, a wide range of raft numbers is examined. Figure 2.13 shows the variation of efficiency and transmission coefficient with nondimensional linear damping coefficient for four raft numbers at $\bar{h} = 1.0$, $\bar{a}_n = 1.0$, $\bar{d} = 0.05$, $\bar{D} = 0.05$ and $\bar{T} = 3.5$. It can be seen that the more rafts a device consists of, the more power could be captured from ocean waves and the less energy could be transmitted to the back of the device. The most visible improvement of power absorption and wave attenuation occurs when the rafts number increases from 2 to 3. When $\bar{c} = 0.05$, the efficiency and the transmission coefficient for the device with 3 rafts are approximately 3.0 and 0.5 times, respectively, as large as those for 2 rafts.

The response curves of efficiency and transmission coefficient with kL for different raft numbers with their corresponding optimal damping coefficients for $\bar{h} = 1.0$, $\bar{a}_n = 1.0$, $\bar{d} = 0.05$ and $\bar{D} = 0.05$ are plotted in Fig. 2.14a, b, respectively. It can be seen that the more the number of rafts adopted in the device is, the higher the main peak of efficiency curve is and the lower the transmission coefficient curve is. It should be also noted that kL corresponding to $\eta = 0$ remains 10.5 for different number of rafts.

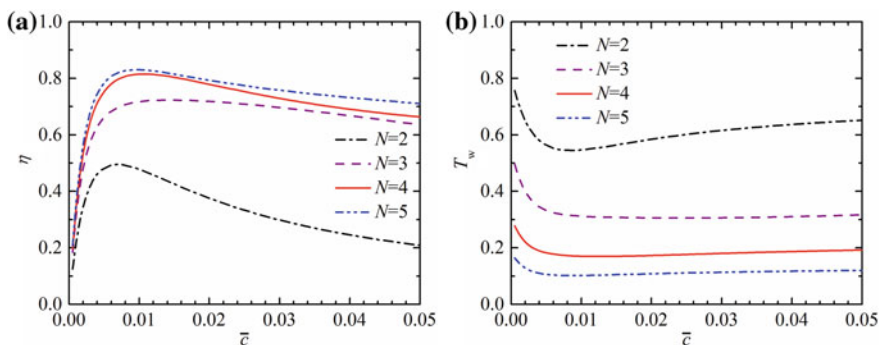


Fig. 2.13 Variation of efficiency and transmission coefficient with nondimensional linear damping coefficient for different raft numbers $\bar{h} = 1.0$, $\bar{a}_n = 1.0$, $\bar{d} = 0.05$, $\bar{D} = 0.05$, $\bar{T} = 3.5$: **a** efficiency; **b** transmission coefficient

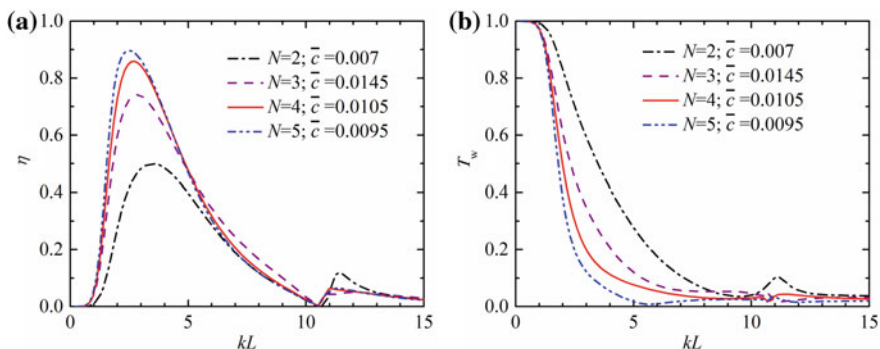


Fig. 2.14 Variation of efficiency and transmission coefficient with nondimensional wave number for different raft numbers with the optimal damping coefficient for $\bar{h} = 1.0$, $\bar{a}_n = 1.0$, $\bar{d} = 0.05$, $\bar{D} = 0.05$: **a** efficiency; **b** transmission coefficient

2.4.5 Raft Length

The effect of raft length on the efficiency and transmission coefficient of the device is also of interest. Figure 2.15 shows the variation of efficiency and transform coefficient with \bar{c} and L/h when $T = 5$ s and $h = 20$ m. It is illustrated from Fig. 2.15a that the efficiency larger than 0.45 can be reached for $L/h = 0.85 \sim 1.55$ with an optimal linear damping coefficient. The rest value of L/h is either too large or too small to make the raft device achieve a high power capture capacity. For a certain wave condition, there is a proper raft length to maximize power absorption. As a comparison, as shown in Fig. 2.15b, the larger the raft length, the smaller the transform coefficient. For a raft device with a infinitely large length, the raft device behaves as a vertical impervious wall and there will be no wave transmitted across the device.

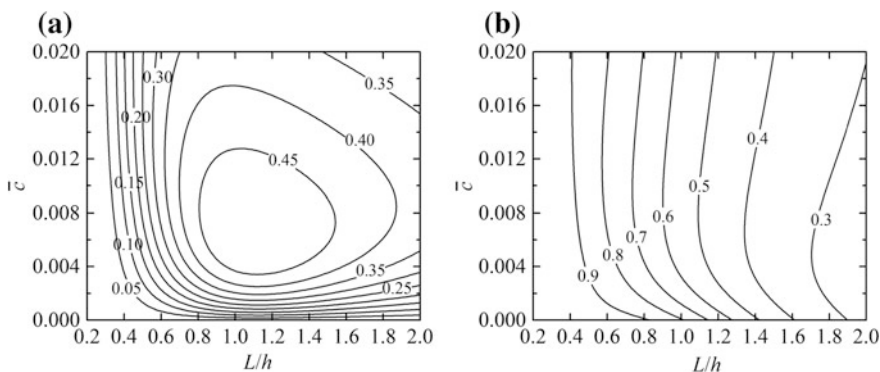


Fig. 2.15 Variation of efficiency and transmission coefficient with L/h and linear damping coefficient for $d_1/h = d_2/h = 0.05$, $D_1/h = 0.05$, $\bar{T} = 3.5$: **a** efficiency contour map; **b** transmission coefficient contour map

2.4.6 Raft Length Ratio

All the previous discussions are carried out based on the premise that all the rafts are of equal length. Figure 2.16 gives the variation of efficiency and transmission coefficient with length ratio, a_1/a_2 , and nondimensional linear damping coefficient for $\bar{h} = 1.0$, $\bar{a}_1 + \bar{a}_2 = 2.0$, $\bar{d} = 0.05$, $\bar{D} = 0.05$ and $\bar{T} = 3.5$. To make it convenient to learn the effect of length ratio, the logarithmic scale is adopted in the horizontal axis as shown in Fig. 2.16. The dash line in the efficiency contour map represents the optimal linear damping coefficient curve in which the corresponding vertical value is the optimal linear damping coefficient to maximize the power absorption of the device with different length ratio. For the device with two same rafts, the efficiency is no more than 0.5, while if the fore raft on wave side is shorter than the aft one in lee side ($a_1/a_2 < 1.0$), more power could be captured from waves. It is shown from Fig. 2.16a that the power capture efficiency is peaked as 0.70 when $a_1/a_2 = 0.35$ and $\bar{c} = 0.0036$, significantly larger than 0.5 for two same rafts ($a_1/a_2 = 1.0$). However, if the fore raft is longer than the aft one ($a_1/a_2 > 1.0$), on the contrary, less power could be absorbed. As a comparison, it is illustrated in Fig. 2.16b that the device with two same rafts ($a_1/a_2 = 1.0$) performs better than those with different rafts length ($a_1/a_2 \neq 1.0$) in attenuating waves.

It is quite interesting to find that the optimal linear damping coefficient curve as shown in Fig. 2.16a and the transmission coefficient contour as shown in Fig. 2.16b are both symmetric about the vertical line $a_1/a_2 = 1.0$. It means that, although there are obvious difference between the wave power capture efficiencies for any two raft devices with inverse a_1/a_2 (just like the same raft device under the waves propagating in opposite directions) as shown in Fig. 2.16a, the optimal linear damping coefficients to maximize power absorption of the two devices are identical and the wave transmission coefficient of these two devices with the same linear damping coefficient are all the same. To the author's knowledge, this finding is revealed here for the first time. The rule behind the symmetry of Fig. 2.16b can be proved analytically, as shown in Appendix A.

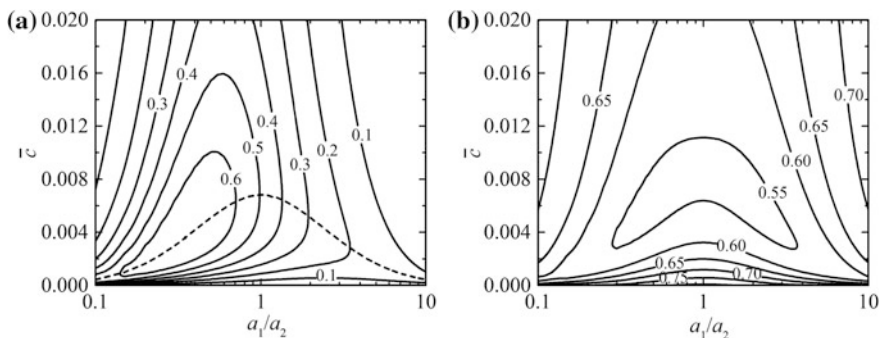


Fig. 2.16 Variation of efficiency and transmission coefficient with a_1/a_2 and nondimensional linear damping coefficient $\bar{h} = 1.0$, $\bar{a}_1 + \bar{a}_2 = 2.0$, $\bar{d} = 0.05$, $\bar{D} = 0.05$, $\bar{T} = 3.5$: **a** efficiency contour map; **b** transmission coefficient contour map

2.5 Summary

In this chapter, an analytical model, based on the linearized velocity potential flow theory, is presented for the motion response, power absorption and wave attenuation of a raft-type wave power device floating on a layer of water of finite depth with waves. Wave excitation forces are calculated directly from incident and diffracted spatial potentials whereas the added masses and damping coefficients for the bodies surging, heaving and pitching in still water are obtained from the corresponding radiated spatial potentials. Motion response, wave power absorption, wave reflection and transmission coefficients of the device are further evaluated. The model is validated by comparison of the present results with published data in terms of: (1) surge and heave excitation; (2) added mass in surge, heave and pitch modes; (3) radiation damping in surge, heave and pitch modes; (4) wave reflection and transmission coefficients; (5) wave power absorption efficiency. In addition, energy conservation equation is also validated. The validated model is then utilized to examine the effect of PTO damping coefficient, raft draft, spacing between two rafts, raft numbers and structure length ratio on power absorption and wave transmission coefficient of raft device. Results reveal that:

- (1) For the raft-type wave power device with two rafts in a certain wave condition, there is a proper raft length and a proper linear damping coefficient to maximize the power absorption, as expected. The larger the raft length, the smaller the transform coefficient.
- (2) A larger spacing distance results in the second peak of the efficiency response curve with a larger peak value. As the spacing distance increases, the second peak efficiency of the raft device and the zero value of efficiency response curves together with the small peak of transmission coefficient are all shifted to lower frequencies.
- (3) For a certain wave condition, the maximum power absorption efficiency of a raft device with the optimal linear damping coefficient will slightly increase first and then decrease dramatically with increasing draft. For long waves, the device with a large draft generally allows less energy to transmit the rafts.
- (4) The more rafts a device consists of, the more power could be captured from ocean waves and the less energy could be transmitted to the back of the device.
- (5) The device consisting of two rafts with different length may be welcome in improving the power capture capacity, while it performs worse than those for two rafts with same length in wave attenuation.
- (6) The same wave transmission coefficient can be obtained by any certain raft-type wave power device, no matter the waves propagate forward or backward.

The analytical model presented in this chapter can be very conveniently used to analyze the characteristics of multiple hinged floats in many other situations, such as effects of pontoon breakwaters and response of connected very large floating

structures. This analytical model is mainly used for hinged floating structures with width obviously larger than wavelength, leading to limitations of wide application of this model.

References

- Falnes J (2002) Ocean waves and oscillating systems: linear interactions including wave-energy extraction, 1st edn. Cambridge University Press, Cambridge
- Haren P (1978) Optimal design of Hagen-Cockerell raft. Dissertation, Massachusetts Institute of Technology
- Koutandos E, Prinos P, Gironella X (2005) Floating breakwater under regular and irregular wave forcing: reflection and transmission characteristics. *J Hydraul Res* 43(2):174–188
- Lamas-Pardo M, Iglesias G, Carral L (2015) A review of Very Large Floating Structures (VLFS) for coastal and offshore uses. *Ocean Eng* 109:677–690
- Li B, Cheng L, Deeks AJ et al (2005) A modified scaled boundary finite-element method for problems with parallel side-faces. Part II. Application and evaluation. *Appl Ocean Res* 27(4–5):224–234
- Liu Y, Li HJ (2014) A new semi-analytical solution for gap resonance between twin rectangular boxes. *Proc Inst Mech Eng, Part M: J Eng Marit Environ* 228(1):3–16
- Lu L, Teng B, Sun L et al (2011) Modelling of multi-bodies in close proximity under water waves —fluid forces on floating bodies. *Ocean Eng* 38(13):1403–1416
- McIver P (1986) Wave forces on adjacent floating bridges. *Appl Ocean Res* 8(2):67–75
- Miao G, Ishida H, Saitoh T (2000) Influence of gaps between multiple floating bodies on wave forces. *China Ocean Eng* 14(4):407–422
- Williams AN, Abul-Azm AG (1997) Dual pontoon floating breakwater. *Ocean Eng* 24(5):465–478
- Williams AN, Lee HS, Huang Z (2000) Floating pontoon breakwaters. *Ocean Eng* 27(3):221–240
- Zhang YL (2010) Fluid-structure dynamic interaction. Academy Press, Beijing
- Zheng S, Zhang Y (2016) Wave diffraction and radiation by multiple rectangular floats. *J Hydraul Res* 54(1):102–115
- Zheng S, Zhang Y (2017) Analytical study on hydrodynamic performance of a raft-type wave power device. *J Mar Sci Technol*, 1–13. doi:[10.1007/s00773-017-0436-z](https://doi.org/10.1007/s00773-017-0436-z)
- Zheng YH, You YG, Shen YM (2004) On the radiation and diffraction of water waves by a rectangular buoy. *Ocean Eng* 31(8–9):1063–1082
- Zheng S, Zhang Y, Sheng W (2015a) Numerical study on the dynamics of a novel two-raft wave energy absorption device. In: *Proceedings of the 11th European Wave and Tidal Energy Conference*, 07C1-3
- Zheng SM, Zhang YH, Zhang YL et al (2015b) Numerical study on the dynamics of a two-raft wave energy conversion device. *J Fluids Struct* 58:271–290

Study on Hydrodynamic Characteristics of the Raft-type
Wave-Powered Desalination Device

Zheng, S.

2018, XVII, 183 p. 115 illus., Hardcover

ISBN: 978-981-10-5516-4